

Fourier-component-engineered metasurfaces support continuous bound states in the continuum and Dirac cone dispersions

Sun-Goo Lee,* Seong-Han Kim, and Chul-Sik Kee†

Integrated Optics Laboratory, Advanced Photonics Research Institute, GIST, Gwangju 61005, South Korea

(Dated: July 2, 2020)

Conventional photonic lattices, including metamaterials and photonic crystals, exhibit various interesting physical properties due to the periodic modulations in lattice parameters. Here, we introduce new types of photonic lattices, namely Fourier-component-engineered metasurfaces, that do not possess the first-order Fourier harmonic component in the periodically modulated lattice parameters, and demonstrate that the metasurfaces support the continuous bound states in the continuum and Dirac cone dispersions near the second stop bands. The concept of engineering Fourier harmonic components in periodic modulations provides a new method to manipulate electromagnetic waves in artificial periodic structures.

Subwavelength photonic lattices with thin-film geometries, such as metasurfaces [1–3] and photonic crystal slabs [4, 5], have attracted significant attention in recent years owing to their substantial abilities of manipulating electromagnetic waves. Unlike the usual thin homogeneous dielectric layers that are governed by the Fresnel equations and Snell’s law [6], photonic lattices can capture the incident light resonantly through the lateral Bloch modes and reemit the light with predesigned electromagnetic responses [7]. By appropriately designing the individual constituents in the lattices, several interesting physical effects and useful applications, which cannot be achieved with conventional dielectric materials, can be realized in an extremely compact format even as a single-layer film [8–10].

Recently, the bound states in the continuum (BICs) and Dirac cone dispersions in planar photonic lattices have been studied extensively. BICs are unusual electromagnetic eigenstates that remain well localized in open photonic systems even though they can coexist with the continuous spectrum of outgoing waves [11–14]. BICs are associated with various fascinating physical phenomena such as the sharp Fano resonances [15], enhanced nonlinear effects [16], and topological nature [17, 18]. Dirac cone dispersion refers to the closed band state with crossing dispersion curves as straight lines in the vicinity of the Γ point at the Brillouin zone center. Dirac cones represent the massless photonic states and are associated with numerous exotic physical features such as the zero-refractive index materials [19–21] and photonic topological insulators [22–24].

Different types of BICs have been studied in versatile planar photonic lattices [25–29]. However, the BICs introduced in the literatures thus far are strongly sensitive to the wavevector of Bloch modes in the lattices. Hence, high- Q Fano resonances due to the BICs can be obtained at a discrete specific incident angle. Small variations in the incident angle significantly reduce the resonance Q factor in the spectral responses. In this letter, we introduce new types of photonic lattices, called Fourier-component-engineered (FCE) metasurfaces, that do not

possess the first-order Fourier harmonic component, and demonstrate that the metasurfaces support continuous BICs in a wide range of wavevectors instead of a specific discrete wavevector. Here, we treat Dirac cones with BICs because the Dirac cones in the vicinity of the Γ point can be accompanied with BICs in planar photonic lattices [30]. With the out-of-plane radiation loss, the Bloch modes exhibit anomalies in the dispersion curves, such as leaky-band flattening and exceptional points, that ruin the Dirac cone dispersion [31, 32].

FCE metasurfaces proposed herein are based on the fact that in the vicinity of the second stop band, radiation loss is caused by the first-order Fourier harmonic component. Figures 1(a) and 1(b) illustrate two of the simplest representative one-dimensional (1D) photonic lattices, i.e., binary dielectric grating (BDG) and zero-contrast grating (ZCG), that support BICs. The periodic modulations in the dielectric constant of BDGs and the variations in thickness of ZCGs generate photonic band gaps at the Bragg condition $k_z = qK/2$, as shown in Fig. 1(c), where k_z is the Bloch wavevector, $K = 2\pi/\Lambda$ is the magnitude of the grating vector, and q is an integer representing the Bragg order. In this study, we focus on the second band gap ($q = 2$) of the fundamental TE_0 mode because BICs and Dirac cones are associated with the second stop bands in many cases. As conceptually illustrated in Fig. 1(d), the second leaky stop band is formed primarily by the direct coupling h_2 with $|\Delta k_z| = 2K$ between two counter propagating waves $\sim \exp(\pm iKz)$, and secondarily by the radiative coupling h_1 with $|\Delta k_z| = K$ between the guided and radiating waves [33].

The coupling processes illustrated in Fig. 1(d) can be clarified by solving the 1D wave equation given by [34]:

$$\left(\frac{\partial^2}{\partial x^2} + \frac{\partial^2}{\partial z^2} \right) E_y(x, z) + \epsilon(x, z) k_0^2 E_y(x, z) = 0, \quad (1)$$

where k_0 denotes the wave number in free space. Equation (1) can be solved by expanding the periodic dielectric function $\epsilon(x, z)$ in a Fourier series and the electric field E_y as a Bloch form [35]. For the 1D lattice BDG shown

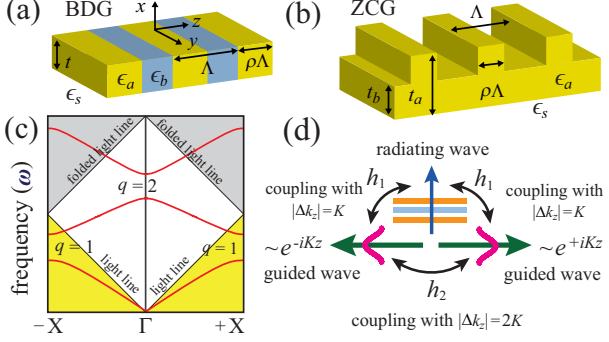


FIG. 1. (a), (b) Schematics of two representative 1D photonic lattices that support BICs. (c) With the periodic modulations in the dielectric constant and thickness, photonic band gaps open at the Bragg condition $k_z = qK/2$. In general, if the lattice supports numerous leaky modes, each mode could also have multiple band gaps. In this study, we focus on the second stop band ($q = 2$) of the fundamental mode. (d) Conceptual illustration of the coupling processes induce the second leaky band gap.

in Fig. 1(a), the dielectric function can be expanded in an even cosine function series $\epsilon(z) = \sum_0^\infty \epsilon_n \cos(nKz)$ where the Fourier coefficients are given by $\epsilon_0 = \epsilon_{avg} = \epsilon_l + \rho\Delta\epsilon$ and $\epsilon_{n\geq 1} = (2\Delta\epsilon/n\pi) \sin(n\pi\rho)$. For clear insight into the formation of the second stop band, we use a simple semianalytical approach in which only the zeroth, first, and second Fourier harmonics are retained for the dielectric function and the spatial electric field distribution is approximated as $E_y(x, z) = [A \exp(+iKz) + B \exp(-iKz)]\varphi(x) + E_{rad}$, where $\varphi(x)$ characterizes the mode profile of the unmodulated waveguide and E_{rad} represents the radiating diffracted wave [36]. Near the second stop band, the dispersion relation can be written as

$$\Omega(k_z) = \Omega_0 - \left(ih_1 \pm \sqrt{k_z^2 + (h_2 + ih_1)^2} \right) / (Kh_0), \quad (2)$$

where Ω_0 is the Bragg frequency under vanishing index modulation, and the coupling coefficients are given by

$$h_0 = \Omega \int_{-\infty}^{\infty} \epsilon_0(x) \varphi(x) \varphi^*(x) dx, \quad (3)$$

$$h_1 = i \frac{K^3 \Omega^4 \epsilon_1^2}{8} \int_{-t}^0 \int_{-t}^0 G(x, x') \varphi(x') \varphi^*(x) dx' dx, \quad (4)$$

$$h_2 = \frac{K \Omega^2 \epsilon_2}{4} \int_{-t}^0 \varphi(x) \varphi^*(x) dx, \quad (5)$$

where $G(x, x')$ denotes the Green's function for the diffracted field [31, 33, 37]. The dispersion relation in Eq. (2), which can be obtained numerically by calculating the coupling coefficients in Eqs. (3)–(5), appropriately describes the second stop band of weakly to moderately modulated photonic lattices. Because the coupling coefficients h_1 and h_2 are formed by the first and second Fourier harmonics, respectively, we can interpret that the

second stop band is formed by the interplay between two coupling processes, as illustrated in Fig. 1(d).

Equation (2) indicates that the leaky stop band with two band edges $\Omega^a = \Omega_0 + h_2/(Kh_0)$ and $\Omega^s = \Omega_0 - (h_2 + i2h_1)/(Kh_0)$ opens at $k_z = 0$. The symmetry-protected BIC appears with the purely real eigenfrequency Ω^a without h_1 at the band edge when the spatial electric field distribution is an asymmetric cosine function ($A = -B$). More, the topologically-protected BICs can be found at the generic k points when the real part of h_1 is zero. A small variation in the lattice parameters moves the position of the topologically-protected BIC along the dispersion curves because $\text{Re}(h_1)$ becomes zero at a slightly different k point with different lattice parameters. The symmetry- and topologically-protected BICs have been studied in several cases in various planar photonic structures. Inspired by the fact that the eigenfrequencies in Eq. (2) become purely real without the contribution of the first-order Fourier harmonic $\epsilon_1 \cos(Kz)$, in this study, we investigate BICs and Dirac cones in the FCE metasurfaces, which do not possess the first-order Fourier harmonic component, that correspond to the representative BDG and ZCG shown in Figs. 1(a) and 1(b), respectively, through the finite element method (FEM) simulations.

In Fig. 2, we first compare the key properties of the conventional BDG and those of the corresponding FCE metasurface. As shown in Fig. 2(a), the FCE metasurface has complex dielectric functions $\epsilon_a - \epsilon_1 \cos(Kz)$ and $\epsilon_b - \epsilon_1 \cos(Kz)$ when $|z| < \rho\Lambda/2$ and $|z| \geq \rho\Lambda/2$, respectively, while the conventional BDG has simple step-like dielectric functions with ϵ_a and ϵ_b in the high and low dielectric constant parts, respectively. Figure 2(b) demonstrates that the second band gap opens at $k_z = 0$ for both the BDG and FCE metasurface and the symmetry-protected BICs appear at the upper band edges. However, the spatial electric field (E_y) distributions in the insets in Fig. 2(b) show that the lower edge mode with the symmetric field distribution in the conventional lattice is radiative out of the lattice, while the lower edge mode in the FCE metasurface is appropriately localized in the lattice. The reduction in the out-of-plane radiation in the FCE metasurface can be observed by investigating the Q factors of the Bloch modes plotted in Fig. 2(c). In the conventional BDG, the symmetry-protected BIC in the upper band exhibits a Q factor that is larger than 10^{15} at the Γ point but the Q values decrease abruptly and approach to the value of Q factor of leaky modes ($\sim 10^3$) in the lower band as k_z moves away from the Γ point. In the FCE metasurface, the symmetry-protected BIC exhibits a Q factor that is larger than 10^{15} and the Q values decrease as k_z moves away from the Γ point. However, the Bloch modes in both the upper and lower band branches have high Q values ($\sim 10^8$) in the computational range of $|k_z| \leq 0.12 K$. The Q factors in the FCE metasurface are approximately 10^5 times larger than those in the BDG with the same lattice parameters

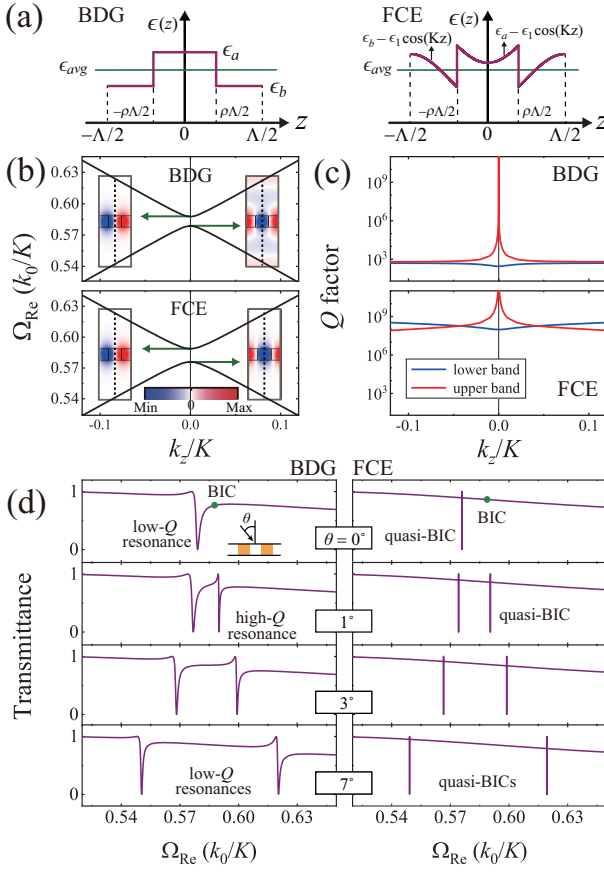


FIG. 2. Comparison between the conventional photonic lattice and FCE metasurface. (a) Dielectric functions as a function of z . (b) FEM simulated dispersion relations near the second stop band. Insets with blue and red colors illustrate the spatial electric field (E_y) distributions of the band edge modes at the $y = 0$ plane. Vertical dotted lines represent the mirror planes in the computational cells. (c) Calculated radiative Q factors of the upper and lower bands. (d) Evolution of transmission spectra vs the incident angle θ . In the FEM simulations, we use the structural parameters $\epsilon_{\text{avg}} = 4.00$, $\Delta\epsilon = 1.00$, $\epsilon_s = 1.00$, $t = 0.50 \text{ \AA}$, and $\rho = 0.40$.

except the profile of the dielectric function.

The symmetry-protected BICs are perfectly embedded eigenvalues with an infinite Q factor and vanishing resonance line width. In diverse practical applications, quasi-BICs with finite high Q values and narrow spectral responses are favorable. Figure 2(d) illustrates the transmission spectra through the BDG and FCE photonic lattices as a function of incident angle θ . At normal incidence with $\theta = 0^\circ$, the BDG structure only exhibits the low- Q resonance by the lower band edge mode. The embedded BIC in the upper band edge mode is not shown in the transmittance curve. When $\theta = 1^\circ$, both the high- Q resonance (quasi-BIC) and low- Q resonance by the upper and lower band Bloch modes, respectively, are observed in the transmittance curve. As θ increases further, the resonance line width by the upper band mode

increases rapidly and becomes close to that by the lower band mode. Two low- Q resonances are observed in the spectral response when $\theta = 7^\circ$. The transmittance curve through the FCE metasurface does not show the embedded BIC in the upper band when $\theta = 0^\circ$. However, the resonance line width by the lower band mode is extremely narrow, unlike the case of conventional BDG. As θ increases from zero, two quasi-BICs by the lower and upper band modes are observed and the resonance line widths remain narrow when $\theta = 7^\circ$. Because the continuous quasi-BICs always exist in the vicinity of the second stop bands of the FCE metasurface irrespective of lattice parameters such as t , $\Delta\epsilon$, and ρ , they could find useful applications to overcome the discrete nature of the BICs in conventional photonic lattices.

Dirac cone dispersions with closed band states, $\text{Re}(\Omega^a) = \text{Re}(\Omega^s)$, can be achieved by adjusting the lattice parameters ρ and/or $\Delta\epsilon$ [31]. Figure 3(a) shows the evolution of the band edge frequencies $\text{Re}(\Omega^a)$ and $\text{Re}(\Omega^b)$ for the conventional BDG and FCE metasurface as a function of ρ . As ρ increases from zero, the band gap opens and its size $|\text{Re}(\Omega^a) - \text{Re}(\Omega^s)|$ first increases, then decreases, and finally becomes zero when $\rho = \rho_c$. The band gap reopens and its size first increases, then decreases, and finally approaches zero when ρ is further increased and approaches 1. At the closed band state with $\rho = \rho_c$, as shown in Fig. 3(b), the dispersion curves of the conventional BDG exhibit a finite range of Bloch wave vectors Δk_z , where $\partial\Omega_{\text{Re}}/\partial k_z \approx 0$. In contrast, the dispersion curves of the FCE metasurface cross as straight lines, and $\partial\Omega_{\text{Re}}/\partial k_z \neq 0$ at $k_z = 0$ at the closed band state. The leaky band flattening in the BDG shown in Fig. 3(b) is evident from the analytical dispersion relations in Eq. (2), which can be rewritten as

$$\Omega(k_z) = \Omega_0 - \left(ih_1 \pm \sqrt{k_z^2 - \text{Re}(h_1)^2} \right) / (Kh_0) \quad (6)$$

at the closed band state with $h_2 = \text{Im}(h_1)$. Equation (6) reveals that leaky band flattening occurs owing

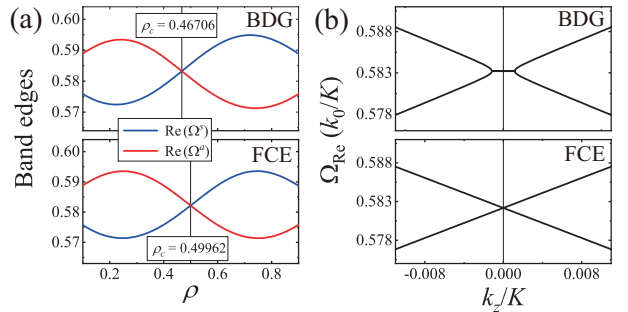


FIG. 3. (a) Simulated band edges for the conventional BDG and FCE metasurface as a function of ρ . Lattice parameters are the same as those for Fig. 2, except that ρ varies. (b) Dispersion relations at the closed band state for the conventional BDG and FCE lattice with $\rho = \rho_c$.

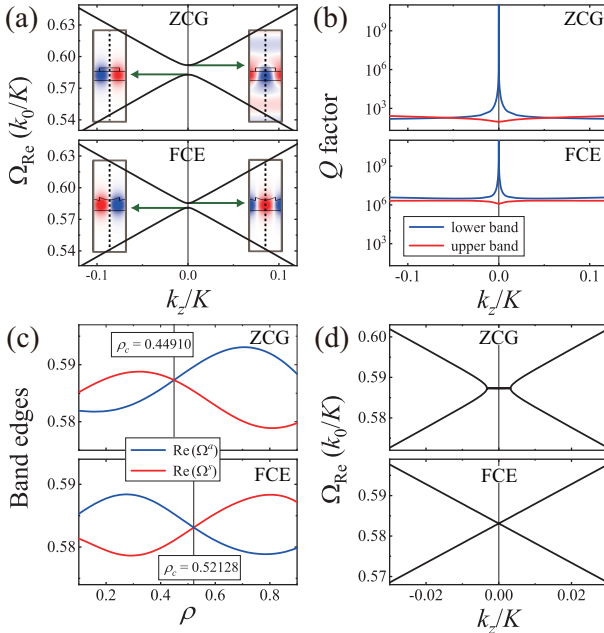


FIG. 4. Simulated dispersion relations (a) and Q factors (b) near the second stop band of the ZCG structure and FCE metasurface. (c) Simulated band edges for the conventional ZCG and FCE metasurface as a function of ρ . For (a), (b), and (c), we use lattice parameters $\Delta t = t_a - t_b = 0.15 \text{ \AA}$, $\rho = 0.60$, $t_{avg} = 0.50 \text{ \AA}$, $t_a = t_{avg} + (1 - \rho)\Delta t$, $\epsilon_a = 4.00$, and $\epsilon_s = 1.00$. (d) Dispersion relations at the closed band state for the conventional ZCG with $\rho_c = 0.44910$ and for the FCE metasurface with $\rho_c = 0.52128$.

ing to the radiative coupling h_1 , and there are exceptional points where the frequency is fully degenerated at $k_z = \pm \text{Re}(h_1)$. Our FEM analysis and the simple dispersion model indicate that the FCE metasurface with continuous BICs could be beneficial in realizing Dirac cone dispersions in planar photonic structures.

BICs and Dirac cone dispersions in the FCE metasurface that correspond to the conventional ZCG structure shown in Fig. 1(b) are investigated next. Because the ZCG exhibits photonic band gaps due to the periodically modulated thickness profile with t_a and t_b in the thick and thin regions, respectively, the corresponding FCE metasurface has thickness profiles $t_a - t_1 \cos(Kz)$ and $t_b - t_1 \cos(Kz)$ when $|z| < \rho\Lambda/2$ and $|z| \geq \rho\Lambda/2$, respectively, where $t_1 = (2\Delta t/\pi) \sin(\pi\rho)$ is the first-order Fourier coefficient. As illustrated in Fig. 4(a), the second band gap opens at $k_z = 0$ for both the ZCG structure and FCE metasurface, and the symmetry-protected BICs appear at the lower band edges, as evident in the spatial electric field distributions in the insets. While the lower edge mode with symmetric field distributions in the ZCG is radiative out of the structure, that in the FCE metasurface is well localized in the lattice. Continuous quasi-BICs due to the absence of the first-order Fourier harmonic component have been illustrated in Fig. 4(b):

they depict the Q factors of the Bloch modes in the upper and lower bands as a function of k_z . In the conventional ZCG, the symmetry-protected BIC in the lower band exhibits a Q factor larger than 10^{15} at the Γ point, but the Q value decreases abruptly and approach the value of the Q factor ($\sim 10^2$) of leaky modes in the upper band as k_z moves away from the Γ point. In the FCE metasurface, the symmetry-protected BIC exhibits a Q factor larger than 10^{15} and the Q value decreases as k_z moves away from the Γ point. However, the Bloch modes in both the upper and lower bands have high Q values, larger than $\sim 10^6$, in the computational range of $|k_z| \leq 0.12 \text{ K}$. The Q factors in the FCE metasurface are approximately 10^4 times larger than those in the ZCG with the same lattice parameters except the thickness profile. Figure 4(c) shows that the closed band states with $\text{Re}(\Omega^a) = \text{Re}(\Omega^s)$ can be achieved by adjusting the lattice parameter ρ for both the ZCG structure and FCE metasurface. At the closed band state with $\rho = \rho_c$, as revealed in Fig. 4(d), the FCE metasurface exhibits the Dirac cone dispersion with $\partial\Omega_{\text{Re}}/\partial k_z \neq 0$ at $k_z = 0$, while the ZCG demonstrates the flat dispersion curves near $k_z = 0$.

In conclusion, we introduced the concept of FCE metasurfaces that do not possess the first-order Fourier harmonic component in the periodically modulated lattice parameters, such as the dielectric constant and thickness, and demonstrated that the new types of lattices support the continuous quasi-BICs and Dirac cone dispersions near the second stop bands. Because the out-of-plane radiation is primarily due to the first-order Fourier harmonic component of the periodic modulation in lattice parameters, the Bloch modes of the FCE metasurface possess high radiative Q factors and there is no leaky band flattening and exceptional point near the second stop bands. Our study is limited to the simplest 1D lattices associated with the first-order Fourier harmonic component. However, the extension of this work to higher-order Fourier harmonics and 2D lattices is feasible.

This research was supported by a grant from the National Research Foundation of Korea funded by the Ministry of Education (No. 2020R1I1A1A01073945) and Ministry of Science and ICT (No. 2020R1F1A1050227), along with the Gwangju Institute of Science and Technology Research Institute in 2020.

* sungooleee@gmail.com

† cskee@gist.ac.kr

- [1] A. V. Kildishev, A. Boltasseva, and V. M. Shalaev, *Science* **339**, 1232009 (2013).
- [2] N. Yu and F. Capasso, *Nat. Mater.* **13**, 139–150 (2014).
- [3] S. Sun, Q. He, J. Hao, S. Xiao, and L. Zhou, *Adv. Opt. Photonics* **11**, 38–479 (2019).
- [4] J. D. Joannopoulos, R. D. Meade, and J. N. Winn, *Pho-*

tonic Crystals: Molding the Flow of Light, (Princeton University, 1995).

[5] G. Johnson, S. Fan, P. Villeneuve, J. D. Joannopoulos, and L. Kolodziejski, Phys. Rev. B **60**, 5751–5758 (1999).

[6] M. Born and E. Wolf, *Principles of Optics*, (Cambridge University Press, Cambridge, 2002).

[7] Y. H. Ko and R. Magnusson, Optica **5**, 289–294 (2018).

[8] A. Arbabi, Y. Horie, M. Bagheri, and A. Faraon, Nat. Nanotechnol. **10**, 937–943 (2015).

[9] A. M. H. Wong and G. V. Eleftheriades, Phys. Rev. X **8**(1), 011036 (2018).

[10] M. Niraula, J. W. Yoon, and R. Magnusson, Opt. Lett. **40**, 5062–5065 (2015).

[11] D. C. Marinica, A. G. Borisov, and S. V. Shabanov, Phys. Rev. Lett. **100**, 183902 (2008).

[12] Y. Plotnik, O. Peleg, F. Dreisow, M. Heinrich, S. Nolte, A. Szameit, and M. Segev, Phys. Rev. Lett. **107**, 183901 (2011).

[13] C. W. Hsu, B. Zhen, A. D. Stone, J. D. Joannopoulos, and M. Soljačić, Nat. Rev. Mater. **1**, 1–13 (2016).

[14] K. Koshelev, G. Favraud, A. Bogdanov, Y. Kivshar, and A. Fratalocchi, Nanophotonics **8**, 725745 (2019).

[15] K. Koshelev, S. Lepeshov, M. Liu, A. Bogdanov, and Y. Kivshar, Phys. Rev. Lett. **121**(19), 193903 (2018).

[16] K. Koshelev, S. Kruk, E. Melik-Gaykazyan, H.-H. Choi, A. Bogdanov, H.-G. Park, Y. Kivshar, Science **367**, 288–292 (2020).

[17] B. Zhen, C. W. Hsu, L. Lu, A. D. Stone, and M. Soljačić, Phys. Rev. Lett. **113**(25), 257401 (2014).

[18] H. M. Doeleman, F. Monticone, W. Hollander, A. Alù, and A. F. Koenderink, Nat. Photonics **12**, 397–401 (2018).

[19] R. W. Ziolkowski, Phys. Rev. E. **70**(4), 046608 (2004).

[20] A. Alù, M. G. Silveirinha, A. Salandrino, and N. Engheta, Phys. Rev. B **75**, 155410 (2007).

[21] I. Liberal and N. Engheta, Nat. Photonics **11**(3), 149–158 (2017).

[22] F. D. M. Haldane and S. Raghu, Phys. Rev. Lett. **100**(1), 013904 (2008).

[23] L. H. Wu and X. Hu, Phys. Rev. Lett. **114**, 223901 (2015).

[24] L. Lu, J. D. Joannopoulos, and M. Soljačić, Nat. Photon. **8**(11), 821–829 (2014).

[25] S. I. Azzam, V. M. Shalaev, A. Boltasseva, and A. V. Kildishev, Phys. Rev. Lett. **121**(25), 253901 (2018).

[26] Y. Yang, C. Peng, Y. Liang, Z. Li, and S. Noda, Phys. Rev. Lett. **113**(3), 037401 (2014).

[27] J. Jin, X. Yin, L. Ni, M. Soljačić, B. Zhen, and C. Peng, Nature **574**, 501–504 (2019).

[28] X. Yin, J. Jin, M. Soljačić, C. Peng, and B. Zhen, Nature **580**, 467471 (2020).

[29] R. Mermel-Lyaudoz, F. Dubois, N. Hoang, E. Drouard, L. Berguiga, C. Seassal, X. Letartre, P. Viktorovitch, and H. S. Nguyen, arXiv:1905.03868 (2019).

[30] M. Minkov, I. A. Williamson, M. Xiao, and S. Fan, Phys. Rev. Lett. **121**, 263901 (2018).

[31] S.-G. Lee and R. Magnusson, Phys. Rev. B **99**(4), 045304 (2019).

[32] B. Zhen, C. W. Hsu, Y. Igarashi, L. Lu, I. Kaminer, A. Pick, S.-L. Chua, J. D. Joannopoulos, and M. Soljačić, Nature (London) **525**, 354–358 (2015).

[33] Y. Ding and R. Magnusson, Opt. Express **15**(2), 680–694 (2007).

[34] A. Yariv and P. Yeh, *Optical Waves in Crystals* (Wiley, New York, 1984).

[35] K. Inoue and K. Ohtaka, *Photonic Crystals: Physics, Fabrication and Applications* (Springer-Verlag Berlin Heidelberg, 2004).

[36] R. F. Kazarinov and C. H. Henry, IEEE J. Quant. Electronics **21**, 144–150 (1985).

[37] D. Rosenblatt, A. Sharon, and A. A. Friesem, IEEE J. Quant. Electronics **33**, 2038–2059 (1997).